NASA/TM—2016-219116

Development of a Subcell Based Modeling Approach for Modeling the Architecturally Dependent Impact Response of Triaxially Braided Polymer Matrix Composites

Chris Sorini and Aditi Chattopadhyay
Arizona State University, Tempe, Arizona

Robert K. Goldberg
Glenn Research Center, Cleveland, Ohio

Lee W. Kohlman
Langley Research Center, Hampton, Virginia

July 2016

NASA STI Program . . . in Profile

Since its founding, NASA has been dedicated to the advancement of aeronautics and space science. The NASA Scientific and Technical Information (STI) Program plays a key part in helping NASA maintain this important role.

The NASA STI Program operates under the auspices of the Agency Chief Information Officer. It collects, organizes, provides for archiving, and disseminates NASA's STI. The NASA STI Program provides access to the NASA Technical Report Server—Registered (NTRS Reg) and NASA Technical Report Server—Public (NTRS) thus providing one of the largest collections of aeronautical and space science STI in the world. Results are published in both non-NASA channels and by NASA in the NASA STI Report Series, which includes the following report types:

- TECHNICAL PUBLICATION. Reports of completed research or a major significant phase of research that present the results of NASA programs and include extensive data or theoretical analysis. Includes compilations of significant scientific and technical data and information deemed to be of continuing reference value. NASA counter-part of peer-reviewed formal professional papers, but has less stringent limitations on manuscript length and extent of graphic presentations.

- TECHNICAL MEMORANDUM. Scientific and technical findings that are preliminary or of specialized interest, e.g., "quick-release" reports, working papers, and bibliographies that contain minimal annotation. Does not contain extensive analysis.

- CONTRACTOR REPORT. Scientific and technical findings by NASA-sponsored contractors and grantees.

- CONFERENCE PUBLICATION. Collected papers from scientific and technical conferences, symposia, seminars, or other meetings sponsored or co-sponsored by NASA.

- SPECIAL PUBLICATION. Scientific, technical, or historical information from NASA programs, projects, and missions, often concerned with subjects having substantial public interest.

- TECHNICAL TRANSLATION. English-language translations of foreign scientific and technical material pertinent to NASA's mission.

For more information about the NASA STI program, see the following:

- Access the NASA STI program home page at http://www.sti.nasa.gov

- E-mail your question to help@sti.nasa.gov

- Fax your question to the NASA STI Information Desk at 757-864-6500

- Telephone the NASA STI Information Desk at 757-864-9658

- Write to:
  NASA STI Program
  Mail Stop 148
  NASA Langley Research Center
  Hampton, VA 23681-2199

NASA/TM—2016-219116

Development of a Subcell Based Modeling Approach for Modeling the Architecturally Dependent Impact Response of Triaxially Braided Polymer Matrix Composites

Chris Sorini and Aditi Chattopadhyay
Arizona State University, Tempe, Arizona

Robert K. Goldberg
Glenn Research Center, Cleveland, Ohio

Lee W. Kohlman
Langley Research Center, Hampton, Virginia

National Aeronautics and
Space Administration

Glenn Research Center
Cleveland, Ohio 44135

July 2016

Level of Review: This material has been technically reviewed by technical management.

Available from

NASA STI Program
Mail Stop 148
NASA Langley Research Center
Hampton, VA 23681-2199

National Technical Information Service
5285 Port Royal Road
Springfield, VA 22161
703-605-6000

This report is available in electronic form at http://www.sti.nasa.gov/ and http://ntrs.nasa.gov/

Development of a Subcell Based Modeling Approach for Modeling the Architecturally Dependent Impact Response of Triaxially Braided Polymer Matrix Composites

Chris Sorini and Aditi Chattopadhyay
Arizona State University
Tempe, Arizona 85281

Robert K. Goldberg
National Aeronautics and Space Administration
Glenn Research Center
Cleveland, Ohio 44135

Lee W. Kohlman
National Aeronautics and Space Administration
Langley Research Center
Hampton, Virginia 23681

Abstract

Understanding the high velocity impact response of polymer matrix composites with complex architectures is critical to many aerospace applications, including engine fan blade containment systems where the structure must be able to completely contain fan blades in the event of a blade-out. Despite the benefits offered by these materials, the complex nature of textile composites presents a significant challenge for the prediction of deformation and damage under both quasi-static and impact loading conditions. The relatively large mesoscale repeating unit cell (in comparison to the size of structural components) causes the material to behave like a structure rather than a homogeneous material. Impact experiments conducted at NASA Glenn Research Center have shown the damage patterns to be a function of the underlying material architecture. Traditional computational techniques that involve modeling these materials using smeared homogeneous, orthotropic material properties at the macroscale result in simulated damage patterns that are a function of the structural geometry, but not the material architecture. In order to preserve heterogeneity at the highest length scale in a robust yet computationally efficient manner, and capture the architecturally dependent damage patterns, a previously-developed subcell modeling approach where the braided composite unit cell is approximated as a series of four adjacent laminated composites is utilized. This work discusses the implementation of the subcell methodology into the commercial transient dynamic finite element code LS-DYNA (Livermore Software Technology Corp.). Verification and validation studies are also presented, including simulation of the tensile response of straight-sided and notched quasi-static coupons composed of a T700/PR520 triaxially braided [0°/60°/–60°] composite. Based on the results of the verification and validation studies, advantages and limitations of the methodology as well as plans for future work are discussed.

Introduction

Polymer matrix composites (PMCs) with complex textile architectures are increasingly being used by the aerospace industry in applications where impact resistance is critical, such as jet engine fan blade containment systems subjected to blade-out events. However, the complex nature of textile composites, particularly braided composites, presents a significant challenge for the prediction of the deformation and damage response of these structures, especially under impact loading conditions. Experimental evidence has shown (Roberts et al. 2002) that when these materials are subjected to impact, oftentimes the damage

will progress along fiber directions. This phenomenon is due to the relatively large repeating unit cell (RUC) in the braided composite as compared to the size of composite structures (Littell 2008). Typically, modeling methodologies that have been developed to simulate the response of textile composites model the composite at the macroscale as a smeared homogeneous, orthotropic material whereby only effective strength and stiffness properties, often obtained through micromechanics-based representative volume element (RVE) approaches, are used (Tanov and Tabiei 2001). However, when smeared homogeneous properties are used in numerical simulations to predict the initiation and propagation of damage, the damage patterns are merely functions of the structural geometry, and the effects of the material architecture are not properly taken into account.

There exists a plethora of research pertaining to the modeling and analysis of textile composites. The analysis methodologies can generally be considered to be either analytical, numerical, or semi-analytical. In the 1980s, Ishikawa and Chou (1982, 1983) attempted to derive an analytical model for 2D woven composites. They proposed three analytical models based on classical laminate theory (CLT), iso-strain, and/or iso-stress assumptions: the mosaic model, the undulation model, and the bridging model. An extension of the undulation model, the "fiber inclination model", was developed by Yang et al. (1986), which allows the derivation of the effective elastic properties based on CLT and an iso-stress assumption. Hahn and Pandey (1994) used a 3D RVE approach to predict the effective moduli and effective thermal expansion coefficients of plain weave fabrics using an iso-strain assumption within the RVE. They accounted for undulations in the warp and weft directions. A different 3D iso-strain model, developed by Shokreih and Mazloomi (2010), was used to predict the stiffness properties of a triaxially braided composite. An in-depth review and comparison of analytical models used to predict the effective properties of textile composites is given by Hallal et al. (2013). Numerical approaches often employ the finite element (FE) method. The determination of material properties for use in structural simulations is often accomplished by explicit modeling of the mesoscale RUC (Tanov and Tabei 2001, and Bednarcyk and Arnold 2003). Multiscale methods that couple micro-, meso-, and/or macroscale simulations have also been developed. Liu et al. (2011) proposed a framework for a three length scale analysis for triaxially braided composites using the generalized method of cells (GMC) micromechanics theory at each length scale. In terms of semi-analytical approaches, Cheng (2006) developed a braiding through the thickness method in which the braided composite is modeled as a series of adjacent laminated composites. This method was later extended by Littell (2008) to account for the nesting of fibers through the composite thickness and has since been improved upon by other researchers (Cheng and Binienda 2008, Li et al. 2009, Goldberg et al. 2011, Xiao et al. 2011, Blinzler 2012, and Cater et al. 2014, 2015).

To account for the effects of the composite architecture on the initiation and propagation of damage in a computationally efficient manner, a semi-analytical subcell-based approach has been developed in which the braided composite is approximated as a series of adjacent laminated composites (Cheng and Binienda 2008, Li et al. 2009, Goldberg et al. 2011, Xiao et al. 2011, Blinzler 2012, and Cater et al. 2014, 2015). The semi-analytical nature of this approach makes it both robust and computationally efficient. The approach has been developed within the context of the commercial transient dynamic finite element code LS-DYNA (Hallquist 2006). In this work, a critical evaluation and verification of this subcell methodology has been conducted. A number of simulations of straight-sided and notched quasi-static tensile coupon tests have been performed for a representative braided composite at a variety of different coupon orientations (0°, 30°, 60°, and 90° with respect to the axial tows). The results of the straight-sided tension coupon simulations are compared to those presented in Cater et al. (2015) and the results of the notched tension coupon simulations are compared to experimental data. It should be mentioned that the ultimate goal of the subcell analysis approach is to model the architecturally dependent damage observed in impact tests (Roberts et al. 2002); the quasi-static coupon simulations in this paper provide insight into the damage mechanisms observed in actual coupon tests and also provide a first test of the analysis method.

Subcell Methodology

The subcell methodology consists of first identifying the braided composite RUC and discretizing it into a series of unique subcell regions depending on the presence of axial and/or braider tows or lack thereof. This approach has currently been designed to analyze triaxially braided polymer matrix composites with a [0°/60°/–60°] braid architecture; future efforts will involve generalizing the methodology such that other triaxially braided fiber architectures as well as other general textile composite architectures can be analyzed. An advantage of the [0°/60°/–60°] layup is that it is quasi-isotropic and has been found to mitigate failures driven by interlaminar stresses (Kohlman 2012 and Cater et al. 2014). An RUC for a typical triaxially braided composite is shown in Figure 1(a), with dimensions shown in Figure 1(b). In Figure 1(a) the red arrow denotes the direction of the axial tows whereas the blue arrows denote the directions of the bias/braider tows. As illustrated in Figure 1(c), the RUC is then discretized into four adjacent subcells. Subcells A and C have a combination of axial tows (red) and braider tows (grey/black) whereas subcells B and D contain only braider tows. Next, each subcell is discretized through its thickness into an approximation of unidirectional (UD) plies with ply layups determined by the braid architecture, as depicted in Figure 1(d). The subcell discretization method shown in Figure 1(d) is known as the absorbed matrix model (AMM) due to the fact that instead of explicitly modeling layers of matrix, the braider plies are assumed to be a homogenized representation of the braider tows and surrounding matrix regions (Cater et al. 2014, 2015). The AMM subcell discretization was found to most accurately represent the in-plane and out-of-plane stiffness properties of the model material in this study (Cater et al. 2015). Following this method, subcells A and C are modeled as antisymmetric composite laminates and subcells B and D are modeled as symmetric composite laminates. The antisymmetry of subcells A and C allows the model to capture tension-twist coupling and localout-of-plane deformations when a specimen is loaded in tension (Cater et al. 2015).

Each subcell is modeled as a discrete laminated composite shell in LS-DYNA. A unit cell thus consists of four adjacent laminated composite shells. By modeling each subcell as its own unique laminate (homogenized through the thickness) instead of homogenizing in the plane of the unit cell, the heterogeneity of the braided composite architecture can be approximated at the macroscale in the finite element model, which will allow for the architecturally dependent damage to be simulated in a manner that balances fidelity and computational efficiency. The next section discusses the procedure for determining the geometric parameters of the subcells.

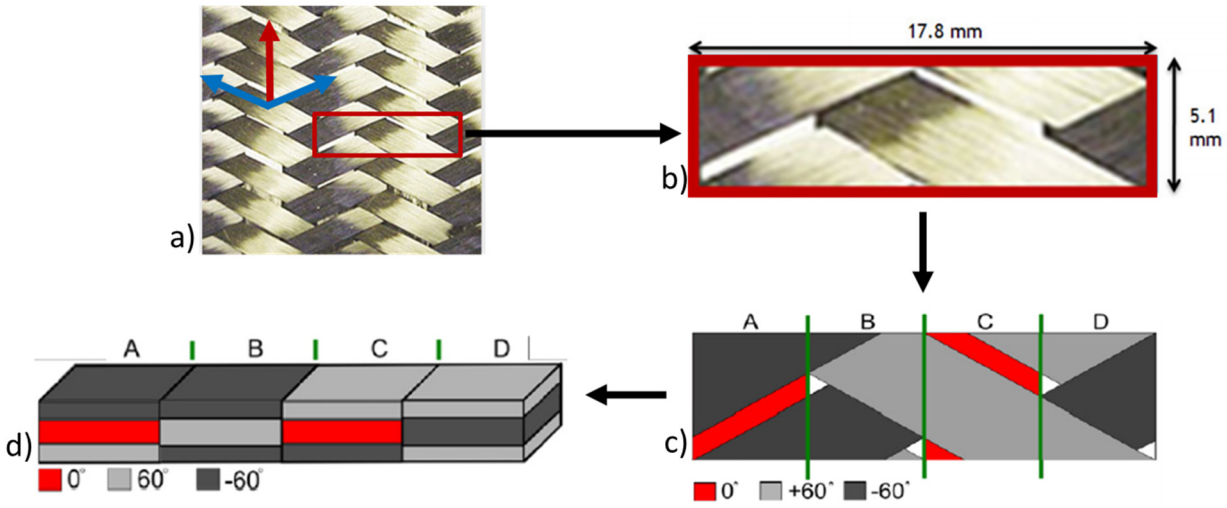

Figure 1.—Illustration of subcell identification and discretization procedure; (a) RUC identification. The red arrow denotes the direction of the axial tows whereas the blue arrows denote the directions of the bias/braider tows; (b) Enlarged image of the identified RUC with dimensions shown; (c) Identification of four adjacent subcell regions; (d) Discretization of each subcell through its thickness into an approximation of unidirectional plies.

Determination of Unidirectional Ply Thicknesses and Fiber Volume Fractions

The first step in the subcell discretization process is to determine the appropriate geometric properties of the subcells. The approach to determine the required parameters is described in detail in Cater et al. (2015) and is summarized here. The primary geometric parameters which need to be determined include the thicknesses of the unidirectional layers that comprise each of the subcells and their respective fiber volume fractions. First, a set of data including the length, width, and height (ply thickness) of a typical RUC and the width of each subcell needs to be determined based on examining micrographs of the braided composite. Additionally, the braid angle, the fiber diameter, and the number of fibers in the axial and braider tows need to be identified, as well as an approximate fiber volume fraction for the fiber tows (axial tows). For this study, a T700/PR520 2D triaxially braided [0°/60°/–60°] composite was examined. This material system has 24 K filaments per tow in the axial (0°) direction, 12 K filaments per tow in the bias/braider (±60° with respect to the axial tows) directions, and six layers of triaxially braided plies through the thickness. The total composite coupon thickness is approximately 3.175 mm, yielding an individual ply thickness of approximately 0.53 mm. Table 1 lists the aforementioned geometric properties for the T700/PR520 material system. Note that the tow fiber volume fraction is (assumed to be) relatively high (80 percent), but this value was selected in order to ensure that the overall fiber volume fraction for the braided composite is appropriately represented (Blinzler 2012).

The volume of axial and braider fibers in subcell A (and C), V_{aA}^{f} and V_{bA}^{f}, as well as the volume of braider fibers in subcells B (and D), V_{bB}^{f}, were computed using the following equations

$$V_{aA}^{f} = \frac{\pi d_a^2}{4} n_a L \tag{1}$$

$$V_{bA}^{f} = \frac{\pi d_b^2}{2} n_b l_{bA} = \frac{\pi d_b^2}{2} n_b \frac{W_A}{\sin(\theta)} \tag{2}$$

$$V_{bB}^{f} = \frac{\pi d_b^2}{2} n_b l_{bB} = \frac{\pi d_b^2}{2} n_b \sqrt{\left(\frac{W_B}{\sin(\theta)}\right)^2 + h^2} \tag{3}$$

TABLE 1.—GEOMETRICAL PARAMETERS FOR THE T700/PR520 MATERIAL SYSTEM USED TO DETERMINE UNIDIRECTIONAL PLY THICKNESSES AND FIBER VOLUME FRACTIONS

Parameter	Description	Value
W_A	Width of subcell A	4.201 mm
W_B	Width of subcell B	4.765 mm
h	Height of RUC	0.53 mm
$V_{f,\text{tow}}$	Fiber volume fraction of axial tows (assumed)	80%
n_a	Number of fibers in axial tow	24 K
n_b	Number of fibers in braider tow	12 K
d_a	Diameter of fiber filaments in axial tows	7 μm
d_b	Diameter of fiber filaments in braider tows	7 μm
L	Length of unit cell	5.1 mm
Θ	Braid angle	±60°

where d_a and d_b are the diameters of the fiber filaments in the axial and braider tows, n_a and n_b are the number of fibers in the axial and braider tows, W_A and W_B are the widths of subcells A and B, h is the height of the unit cell, θ is the braid angle, L is the length of the unit cell, l_{bA} is the length of the braider tows in subcell A (and C), and l_{bB} is the length of braider tows in subcell B (and D). The lowercase subscripts refer to the axial/braider tows whereas the uppercase subscripts refer to the respective subcell. Figure 2 helps to illustrate some of the aforementioned geometric properties required for the analysis. In the figure, the yellow boxes represent the volume of a single braider tow within a subcell whereas the green boxes represent the total subcell volume. Figure 3 illustrates the method developed by Xiao et al. (2011), where the braider tow lengths are approximated as straight lines. Table 2 summarizes the calculated total volume of axial and braider fibers in each subcell.

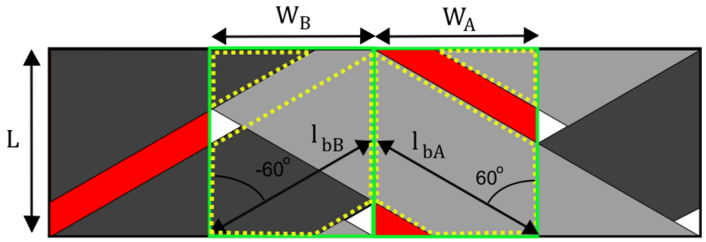

Figure 2.—Schematic illustrating the lengths/volumes of the braider tows in subcells A and B.

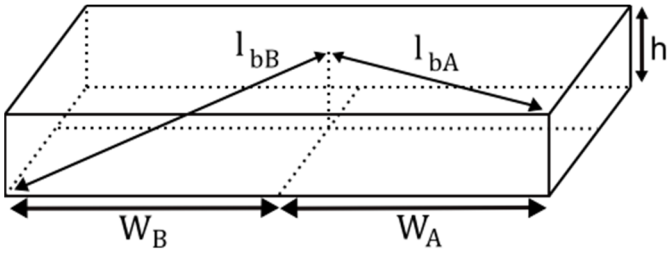

Figure 3.—Schematic of the straight-line model used to determine bias tow lengths.

TABLE 2.—TOTAL VOLUME OF AXIAL AND BRAIDER FIBERS IN EACH SUBCELL

Subcell	Total volume of bias fibers (m^3)	Total volume of axial fibers (m^3)
A/C	4.48×10^{-9}	4.71×10^{-9}
B/D	5.11×10^{-9}	0

The thickness of the axial plies in subcell A (and C), V_{aA}, with respect to total subcell thickness is then computed based on the assumed axial tow fiber volume fraction ($V_{f,\text{tow}}$) of 80 percent, the volume of fibers in subcell A (and C), V_{aA}^{f}, as well as the length, width, and height of subcell A (and C) using Equation (4). Since the rest of subcell A (and C) must be made up of braider tows, the thickness of each of the bias tows in subcell A (and C) is calculated according to Equation (5).

$$V_{aA} = \frac{V_{aA}^{f}}{V_{f,tow} W_A h L} \tag{4}$$

$$V_{bA} = \frac{1 - V_{aA}}{2} \tag{5}$$

It should be mentioned that the thicknesses of the UD layers of subcell B (and D), which only contains braider tows, are determined based on the assumption that there is an equal amount of ±60° braider tows present in subcell B (and D). Lastly, the fiber volume fractions of the braider tows in subcells A (and C) and B (and D), $V_{f,bA}$ and $V_{f,bB}$, are calculated using Equations (6) and (7).

$$V_{f,bA} = \frac{V_{bA}^{f}}{V_{bA} W_A h L} \tag{6}$$

$$V_{f,bB} = \frac{V_{bB}^{f}}{V_{bB} W_B h L} \tag{7}$$

Table 3 shows a summary of the calculated fiber volume fractions and UD ply thicknesses for each of the subcells. It can be seen that the only difference between subcells A and C (and likewise between B and D) are the UD layer orientations (braid angles). Moreover, it is important to note that there are three unique fiber volume fractions (37.5, 73.3, and 80 percent) corresponding to three unique UD ply regions.

TABLE 3.—SUMMARY OF CALCULATED FIBER VOLUME FRACTIONS AND UD PLY THICKNESSES]

Subcell A layup	Braid angle	Fiber V_f (%)	Thickness (%)[a]
Braider tow	–60°	73.3	25.5
Axial tow	0°	80	49
Braider tow	+60°	73.3	25.5
Subcell B layup	Braid angle	Fiber V_f (%)	Thickness[a]
Braider tow	–60°	37.5	25
Braider tow	+60°	37.5	50
Braider tow	–60°	37.5	25
Subcell C layup	Braid angle	Fiber V_f (%)	Thickness (%)[a]
Braider tow	+60°	73.3	25.5
Axial tow	0°	80	49
Braider tow	–60°	73.3	25.5
Subcell D layup	Braid angle	Fiber V_f (%)	Thickness[a]
Braider tow	+60°	37.5	25
Braider tow	–60°	37.5	50
Braider tow	+60°	37.5	25

[a]Shown as a percent of overall subcell thickness.

Material Model

To model the constitutive response of the various plies within each of the subcells, the LS-DYNA material model MAT_058 (Laminated Composite Fabric) was employed. MAT_058 is a continuum damage mechanics (CDM) model that utilizes the Hashin failure criterion in which the failure envelope is a function of the longitudinal tensile and compressive strengths, transverse tensile and compressive strengths, and shear strengths (Hashin 1980 and Matzenmiller 1995). MAT_058 uses an exponential damage evolution in which the damage parameters in the longitudinal, transverse, and shear directions control the degradation of the elastic properties and thus allow nonlinearity in the stress-strain response. Equation (8) shows the constitutive matrix as a function of damage in the longitudinal (ω_{11}), transverse (ω_{22}), and shear (ω_{12}) directions.

$$C(\omega) = \frac{1}{D}\begin{bmatrix} (1-\omega_{11})E_{11} & (1-\omega_{11})(1-\omega_{22})\nu_{21}E_{22} & 0 \\ (1-\omega_{11})(1-\omega_{22})\nu_{12}E_{11} & (1-\omega_{22})E_{22} & 0 \\ 0 & 0 & D(1-\omega_{12})G_{12} \end{bmatrix} \quad (8)$$

$$where\ D = 1-(1-\omega_{11})(1-\omega_{22})\nu_{12}\nu_{21}$$

The damage parameters range between zero (undamaged) and one (fully damaged). Once a damage parameter reaches a value of unity in a particular direction, various stress limiting parameters allow the specification of a post-failure "plateau" stress as a percentage of the maximum stress in the particular coordinate direction. The tensile and compressive stress limiting parameters in the longitudinal direction, SLIMT1 and SLIMC1, were both chosen to be 0.01 in Cater et al. (2015) in order to prescribe brittle failure in the fiber directions. In this study, it was found that SLIMT1 and SLIMC1 parameters of 0.3 and 0.1 work best to correlate to the experimental test data for *both* straight-sided and notched tensile coupon tests. All of the other stress limiting parameters were set to one. MAT_058 also allows the specification of the maximum effective strain an element can experience before erosion (deletion) occurs. In this study, no element erosion is used; all nonlinearity in the stress-strain curves is solely due to degradation of the elastic constants.

Since the Hashin (1980) failure criterion is based on five stresses and the corresponding strain values, a total of ten strength (and corresponding strain) values need to be specified for each MAT_058 material definition. There are a total of three material definitions; one for each unique UD ply region/fiber volume fraction (see Table 3), which means each model requires 30 parameters to characterize the strength of the material (note this excludes moduli, stress limiting parameters, etc.). The next section discusses the process for populating the required input parameters of MAT_058 (strength and stiffness) using a combination of top-down and bottom-up techniques.

Bottom-Up Micromechanics Approach to Determine Unidirectional Ply Stiffness

Due to the processing methods used for braided composites, equivalent UD coupons for physical testing cannot be manufactured; therefore a bottom-up micromechanics approach is utilized to determine the stiffness properties of the three unique UD ply regions identified for the braided composite. MAC/GMC (Bednarcyk and Arnold 2002), a Micromechanics Analysis Code (MAC) developed at NASA Glenn Research Center based on the Generalized Method of Cells (GMC) (Paley and Aboudi 1992), was employed in conjunction with a nonlinear, strain rate dependent polymer constitutive model (Goldberg et al. 2003), which incorporates hydrostatic stress effects, to compute the UD ply stiffness properties for this study. These properties were computed based on the fiber volume fractions of the respective UD ply regions, computed using the procedures described earlier, and the constituent properties, which were obtained from Cater et al. (2015) and can be seen in Table 4. The resulting effective UD stiffness properties for the three unique ply regions in the T700/PR520 braided composite are shown in Table 5.

TABLE 4.—ELASTIC PROPERTIES FOR T700 FIBERS AND PR520 MATRIX

Material	Density (g/cm^3)	E_{11} (GPa)	E_{22} (GPa)	G_{12} (GPa)	ν_{12}
T700 (Fiber)	1.8	230	15	27	0.2
PR520 (Matrix)	1.25	4	4	1.44	0.38

TABLE 5.—EFFECTIVE PLY STIFFNESS PROPERTIES FOR THREE UNIQUE SUBCELL REGIONS PREDICTED BY MAC/GMC

Description	UD *Vf* (%)	E_{11} (GPa)	E_{22} (GPa)	E_{33} (GPa)	G_{23} (GPa)	G_{13} (GPa)	G_{12} (GPa)	ν_{12}
B/D-braider	37.50	88.5	6.5	6.5	1.9	2.2	2.4	0.3
A/C-braider	73.30	169.5	10.5	10.5	3	5.25	5.25	0.23
A/C-axial	80	184.7	11.4	11.4	3.5	11.2	6.29	0.24

Top-Down Unit Cell Approach to Determine Longitudinal Tensile and Compressive Ply Strengths

The process to determine the longitudinal tensile and compressive strengths of the axial UD plies (with 80 percent fiber volume fraction) utilized the top-down unit cell approach discussed in Cater et al. (2015) and summarized here. Using this approach, the strength properties are "backed-out" based on straight-sided coupon level test data. The advantage of this type of approach is that the in-situ behaviors of the composite are implicitly accounted for in the determination of the equivalent ply level strengths. Note this approach assumes the coupon response is linear elastic until failure. In the application of this method, the relevant macroscopic failure modes are linked to the failure of a particular unidirectional ply. For example, in order to determine the longitudinal tensile strength of the axial plies, a coupon level test that exhibited a tensile failure of the axial tows needs to be identified. The failure mode of straight-sided axial tension tests was identified to be a tensile failure of the axial tows (Kohlman 2012). A single RUC was then modeled in LS-DYNA, subjected to periodic boundary conditions, and loaded in tension in the axial direction until an overall stress level equal to the macroscopic failure strength was reached. The longitudinal stress in the UD layer representing the axial ply was then determined and set to be the ultimate longitudinal tensile strength of the axial ply. The same unit cell approach was used to determine the longitudinal compressive strength of the axial tows. To determine the longitudinal compressive strength of the bias tows, a similar process was utilized based on coupon level transverse compression tests. Since the bias tows were the dominant plies carrying the load during transverse compression tests, this process was deemed to be acceptable. Due to the complexity of linking the longitudinal tensile failure of the bias tows (in straight-sided tension experiments) to a specific macroscopic loading condition, the longitudinal tensile strengths of the bias plies in subcells A/C and B/D (fiber volume fractions of 73.3 and 37.5 percent) were determined by making the assumption that the failure strain was equal to that of the axial plies (approximately 1.9 percent). Assuming a linear elastic response along the fiber direction, the failure strain was multiplied by the effective longitudinal modulus of the bias plies to determine the axial tension failure strength of the bias plies. The computed MAT_058 input axial tow strength values (XT for longitudinal tension and XC for longitudinal compression) for the T700/PR520 composite examined in this study are listed in Table 6, and the input axial tow failure strain values (E11T for longitudinal tension and E11C for longitudinal compression) are listed in Table 7.

TABLE 6.—SUMMARY OF STRENGTHS FOR THE THREE UNIQUE UD PLY REGIONS

	UD Ply strength (MPa)					
	XT	XC	YT	YC	SC	TAU1
Axial plies (V_f = 80%)	3599	1379	151	218	218	200
A/C braider plies (V_f = 73.3%)	3302	696	135	221	221	201
B/D braider plies (V_f = 37.5%)	1725	403	87.7	193.4	193.4	75

TABLE 7.—SUMMARY OF FAILURE STRAINS FOR THE THREE UNIQUE UD PLY REGIONS

	UD failure strain					
	E11T	E11C	E22T	E22C	GMS	GAMMA1
Axial plies (V_f = 80%)	0.0195	0.0075	0.0182	0.0191	0.1475	0.0750
A/C braider plies (V_f = 73.3%)	0.0195	0.0045	0.0200	0.0211	0.1600	0.0840
B/D braider plies (V_f = 37.5%)	0.0195	0.0041	0.0300	0.0295	0.3000	0.0450

Bottom-Up Micromechanics Approach to Determine Transverse Tensile Strength and Shear Strength

The "top-down" method described could not be utilized to obtain the additional required strength parameters (transverse tension, transverse compression and shear) for the equivalent axial and bias plies because these local failure modes could not be easily correlated to the results of coupon level tests of the braided composite. Furthermore, the equivalent ply level response in the transverse and shear directions was assumed to be nonlinear, which violated the assumptions of linear elasticity utilized above. Once again, the procedure described here is a summary of the detailed methodology described in Cater et al. (2015). MAC/GMC was utilized again with the aforementioned polymer constitutive model (Goldberg et al. 2003) to create equivalent transverse tension and shear stress-strain curves for each of the three equivalent plies used to model the braided composite. LS-DYNA simulations of the stress-strain response of the appropriate plies were then conducted, and the appropriate input parameters in MAT_058 were adjusted until the LS-DYNA simulation results correlated reasonably well to the curves generated using MAC/GMC. For the T700/PR520 composite examined in this study, the transverse tensile strengths and corresponding failure strains were determined from the plots in Figure 4(a) to (c) and are denoted

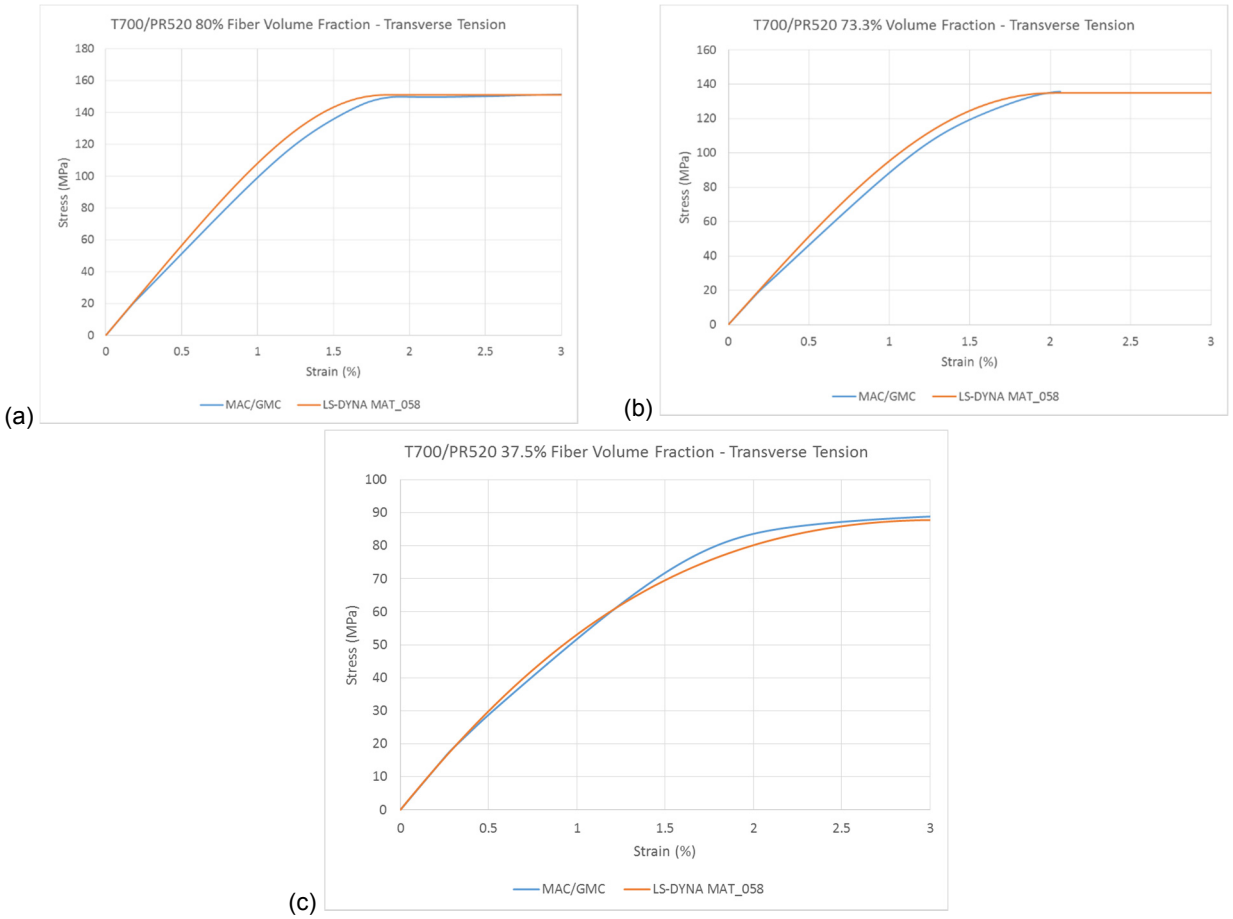

Figure 4.—Stress-strain curves for transverse tension simulations for the three unique UD ply regions, both generated with MAC/GMC and LS-DYNA MAT_058; (a) 80 percent fiber volume fraction; (b) 73.3 percent fiber volume fraction; (c) 37.5 percent fiber volume fraction.

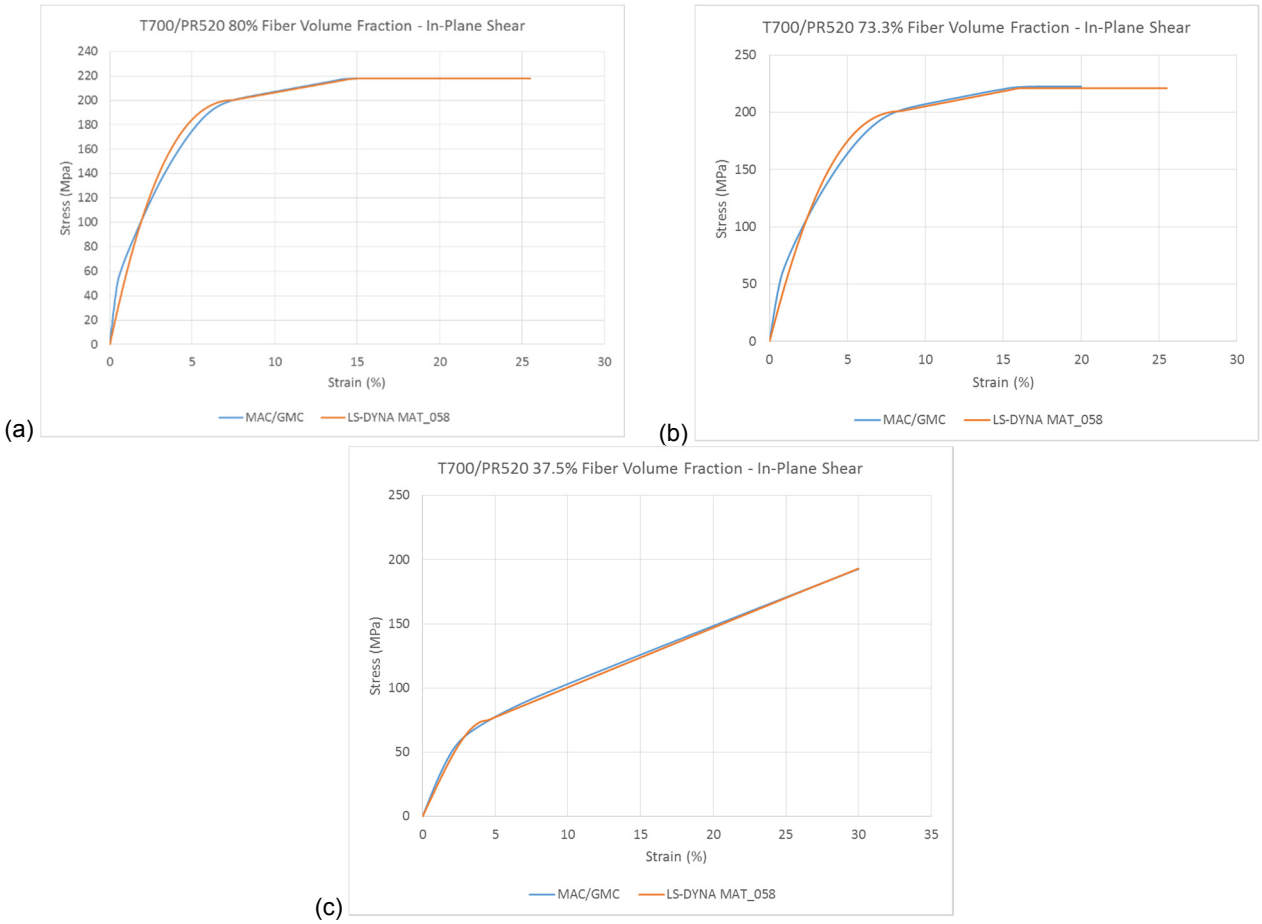

Figure 5.—Stress-strain curves for in-plane shear simulations for the three unique UD ply regions, both generated with MAC/GMC and in LS-DYNA; (a) 80 percent fiber volume fraction; (b) 73.3 percent fiber volume fraction; (c) 37.5 percent fiber volume fraction.

"YT" and "E22T" in Tables 6 and 7. The shear strength as well as the stress at the point in which slight nonlinearity in the material response became apparent, along with the corresponding strains, were determined from the graphs in Figure 5(a) to (c) and are denoted "SC", "TAU1", "GAMMA1", and "GMS", respectively, in Tables 6 and 7. Transverse compressive failure of the bias tows was not a failure mode observed in experiments, thus limiting the ability of properly characterizing these strength parameters. Furthermore, the MAC/GMC simulations did not yield nonlinear stress-strain curves in a form that could easily be correlated to equivalent LS-DYNA simulations. As a result, the transverse compressive strengths of the bias tow ply regions in subcells A/C and B/D (fiber volume fractions of 73.3 and 37.5 percent) were set equal to the (relatively high) in-plane shear strengths and the strengths were divided by the appropriate transverse modulus to obtain the failure strain. The transverse compressive failure stress (YC) and corresponding failure strain (E22C) are listed in Tables 6 and 7.

Straight-Sided Coupon Simulation Results

To verify and validate the subcell analysis method, a series of straight-sided quasi-static tensile coupon tests were simulated and compared to experimental data. The physical experiments were performed using an MTS servo hydraulic load frame under displacement control at a displacement rate of 1.27 mm/min. The physical straight-sided coupons under investigation were 304.8 mm in length, 35.8 mm in width, and 3.175 mm in thickness. The load frame gripped 50.8 mm on each end of the coupons (with no tabbing used), leaving a 203.2 mm gage length. Coupon tests with various off-axis

angles of loading with respect to the direction of the axial tows were considered: 0°, 30°, 60°, and 90°. The standard axial (0°) and transverse (90°) tension tests load the coupons in directions parallel and perpendicular to the axial tows whereas the 60° and 30° off-axis tension tests load the coupons in directions parallel and perpendicular to the bias tows, thus providing more useful data for validation and fine-tuning of the subcell model parameters. Note that at this stage of the analysis, it is primarily the stress limiting parameters that need to be fine-tuned to match the experimental material response. As mentioned previously, stress limiting parameters for longitudinal tension (SLIMT1) and compression (SLIMC1) of 0.3 and 0.1 were found to best match *both* the straight-sided and notched (to be discussed later) experimental data in this study. All other stress limiting parameters have been set to one. The same stress limiting parameters have been used for the material definition of each of the three unique UD ply regions.

Each of the subcells was modeled in LS-DYNA as a discrete laminated composite using Belytschko-Tsay composite shell elements. The UD plies are represented by integration points stacked through the thickness of the shell elements using INTEGRATION_SHELL cards to specify the layup and SECTION_SHELL cards to specify the integration layer orientations. Figure 6 shows the RUC in LS-DYNA and illustrates how each subcell is modeled as its own laminated composite shell. As previously mentioned, the physical T700/PR520 coupons considered in this study have six layers of triaxially braided plies through the thickness.

In previous works (Cater et al. 2014, 2015), it was found that the transverse (90°) modulus and the effects of locally antisymmetric regions (i.e., subcells A and C) were better captured by modeling the coupons with six layers of shell elements, each with three integration layers, through the thickness (yielding a total of 18 integration points through the thickness) and a contact algorithm to tie the slave nodes of each of the shell layers to the master segments of adjacent shell layers. Cater et al. (2014) stated that modeling composites with multiple layers of ply reinforcement with one layer of shell elements through the thickness may yield an inadequate representation of the transverse and out-of-plane responses. However, preliminary impact simulations (to be discussed in future works) revealed that models with multiple layers of shell elements through the coupon thickness yielded a nonphysical impact response due to the contact algorithm. Furthermore, the contact algorithm used in the six layer models in Cater et al. (2015), CONTACT_TIED_SHELL_EDGE_TO_SURFACE_BEAM_OFFSET, had to be correlated to match the experimental data, effectively introducing several ad-hoc parameters into the analysis (an in-depth investigation of different contact algorithms is presented in Cater et al. (2015)). Since the final goal of this research is to simulate impact, all models in this study use a single through-thickness layer of shell elements, each with 18 integration layers. Note that there are some minor discrepancies between the results presented in this paper and the results presented in Cater et al. (2015) due to this change, which will be discussed in this section, however this slight loss in accuracy in simulating quasi-static coupon tests was deemed acceptable in order to allow the method to work properly for impact simulations.

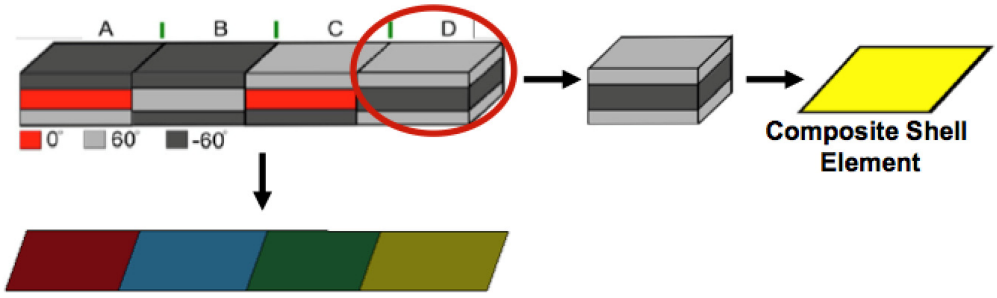

Figure 6.—Schematic illustrating the implementation of the subcell methodology into LS-DYNA.

In Cater et al. (2015), two different stacking arrangements of the RUC through the composite thickness were considered, “perfect stack” and “ideal shift”. The prior considers a perfect stacking of axial tows through the thickness of the composite whereas the latter considers a stacking in which every other integration layer is shifted by the width of subcell A/C. The ideally shifted integration layup is used in this study in order to approximate the observed nesting in physical specimens. Figure 7 shows a schematic of the ideally shifted integration layup whereas Figure 8 illustrates the actual nesting in the physical coupons which the ideally shifted integration layup intends to approximate. Note that by modeling the coupons in this study with a single through-thickness layer of shell elements, each with 18 integration layers, and approximating the nesting observed in physical coupons with the ideally shifted integration layup, subcells B and D are no longer modeled as symmetric laminates.

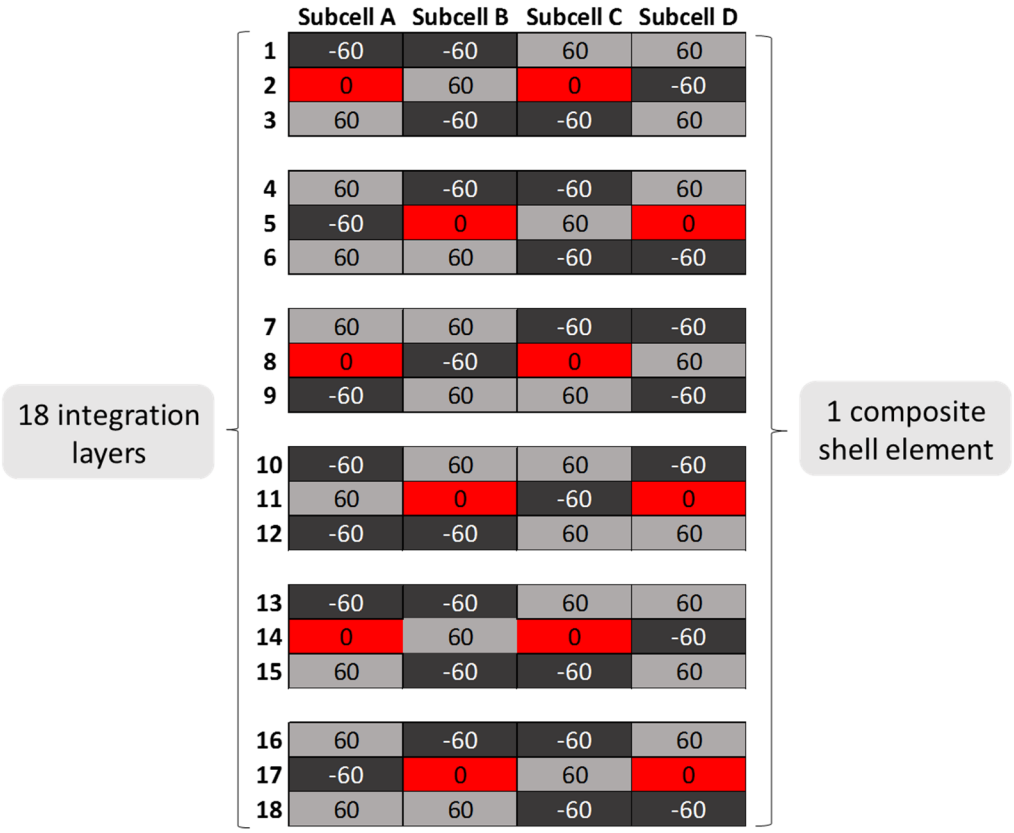

Figure 7.—Schematic of the ideally shifted integration layup.

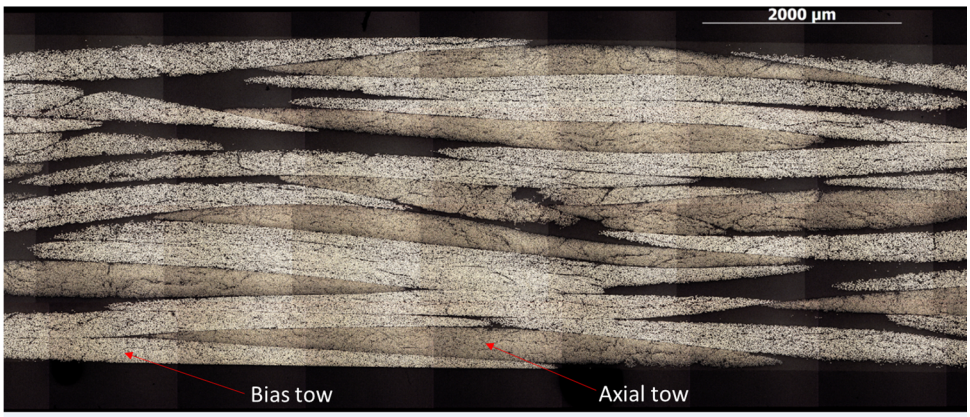

Figure 8.—Microscopy image showing the nesting of axial tows through the thickness in the T700/PR520 material system.

The finite element meshes of the coupons for the 0°, 30°, 60°, and 90° straight-sided tension simulations are shown in Figure 9(a) to (d) and the simulated stress-strain curves are shown in Figure 10(a) to (d). It should be emphasized that the post-peak stress-strain response seen in Figure 10(a) to (d) is primarily numerical artifact, and thus may not be representative of the actual material response. However, the choice was made to include the post-peak response in the stress-strain curves to potentially provide insight into the residual strength of the coupons. Notice in the finite element models shown in Figure 9(a) to (d), only the axial tows are continuous. The mesh generation of the 30° and 60° coupons followed the approach by Cater et al. (2015), where a skewed mesh was used to preserve axial tow continuity and to maintain a flat edge in the FE coupon geometry. In previous subcell research (Cheng and Binienda 2008, Li et al. 2009, Goldberg et al. 2011, Xiao et al. 2011, Blinzler 2012, and Cater et al. 2014, 2015), the dimensions of the elements had physical significance in that each subcell was represented by one element. However, in order to create analysis models of notched coupon tests (discussed later) with appropriate geometry, a smaller mesh size needed to be used. If smaller elements were only used near the notch, damage would localize in these elements because, when possible, strain localization phenomena (such as damage) tends to localize in the smallest element in a finite element mesh (Pijaudier-Cabot and Bazant 1987 and Schwer 2011). To facilitate comparison of the straight-sided and notched coupon results, the said smaller mesh size was also used for the straight-sided coupon meshes.

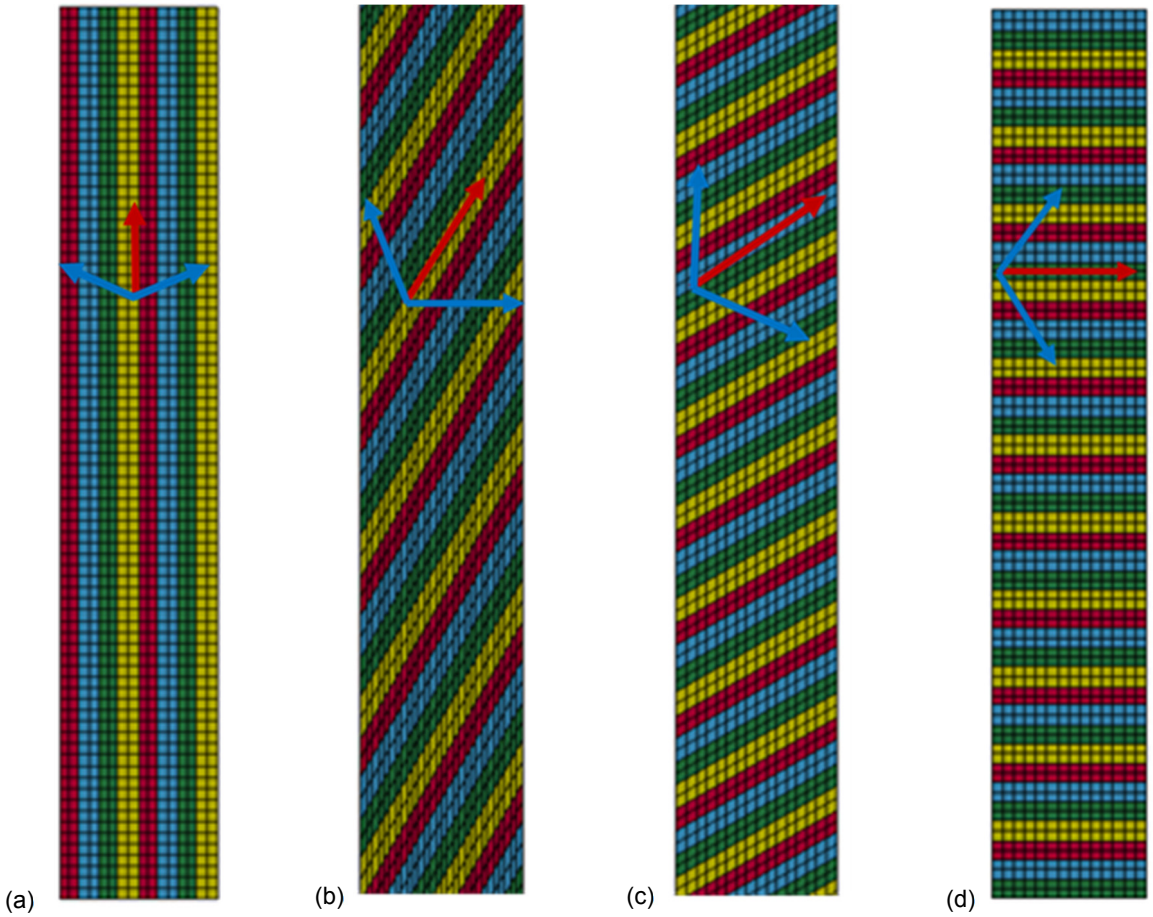

Figure 9.—Finite element models of the (a) 0°, (b) 30°, (c) 60°, and (d) 90° straight-sided coupons created in LS-DYNA. The directions of the axial and bias tows are denoted by the red and blue arrows, respectively.

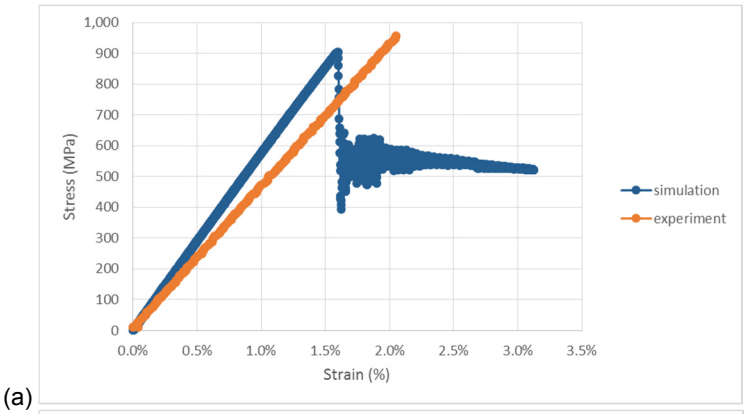

(a)

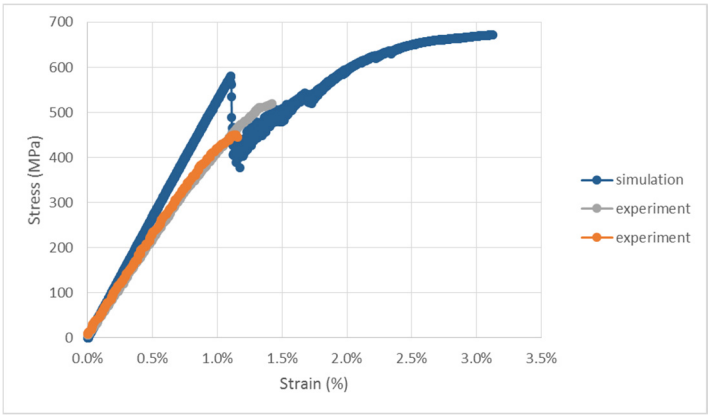

(b)

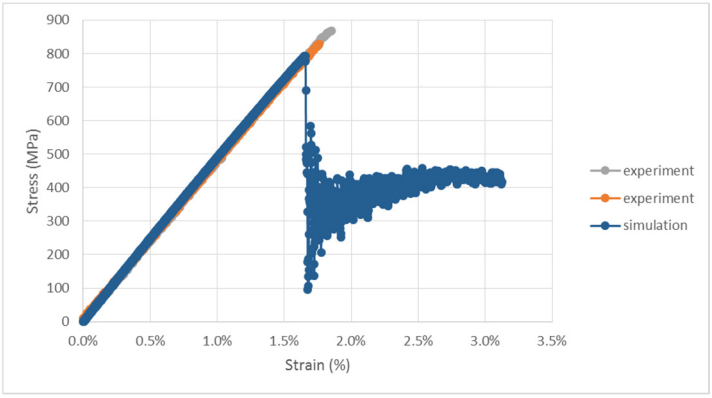

(c)

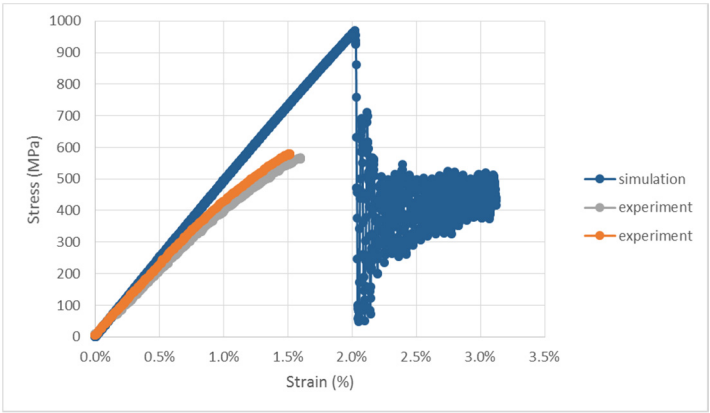

(d)

Figure 10.—Stress-strain curves for straight-sided coupon simulations; (a) 0° axial tension; (b) 30° off-axis tension; (c) 60° off-axis tension; (d) 90° transverse tension.

The simulated stress-strain curve for the axial tension response of the 0° coupon as well as the experimental data can be seen in Figure 10(a). The predicted strength of 904 MPa (the simulated stress when the load drop occurred) correlates well to the experimentally observed strength of 984 MPa, however the predicted modulus is higher than that observed in the experiment and that predicted by Cater et al. (2015), which was very close to the experimentally measured modulus. This increase in modulus was observed in changing from six layers of shell elements through the thickness, each with three integration points, to one shell element through the thickness with 18 integration points. It is likely due to the CONTACT_TIED_SHELL_EDGE_TO_SURFACE_BEAM_OFFSET contact algorithm mentioned previously, which allows translational and rotational degrees of freedom (which can be controlled by various ad-hoc parameters) between the slave nodes and master segments. With one layer of shell elements through the thickness, these translational and rotational degrees of freedom are no longer present (because there is only one layer), thus increasing the simulated coupon stiffness.

The predicted failure mode of the 0° coupon is a tensile failure of the axial plies, which is in agreement with the observed experimental failure mode, identified in Cater et al. (2015) to be a longitudinal tensile failure of the axial tows. This is supported by the fact that, in the simulation, integration layers representing axial tows reached their damaged value of unity in the longitudinal direction before any of the other integration layers and also due to the fact that the axial tows carry the majority of the load prior to the simulated failure. Figure 11 shows contours of stress in the (local) longitudinal direction; the local longitudinal direction of the axial plies is vertical in this case. The yellow/orange/red elements in the contour plot belong to integration points that represent axial tows, indicating the axial tows carry the majority of the applied loading prior to failure. The maximum stress value of 3599 MPa, which is equal to the ultimate strength (XT) specified for the axial tows, occurs in the axial tows near the grips (gripped nodes at the ends of the coupon). The failure occurred near the grips in the simulation, which may be partially due to boundary conditions, whereas Cater et al. (2015) reported the experiments to fail at the grips and in the gage section. Note how the experimental stress-strain curve cuts off suddenly; this is due to the load frame experiencing a stop condition due to a sudden drop in load. On the other hand, the simulated stress-strain curve plateaus between 500 and 600 MPa after the initial load drop. In the simulation, the majority of the load is still carried by what remains of the axial tows post-failure. The stress limiting parameter SLIMT1 (taken as 0.3 in this work) allows the failed axial tows to carry 30 percent of the specified XT value (see Table 6) after they have failed in longitudinal tension. Cater et al. (2015) stated that the experimental axial tension coupons had very little residual coupon strength (based on qualitative inspection); thus, the post-peak response of the 0° may be primarily numerical artifact.

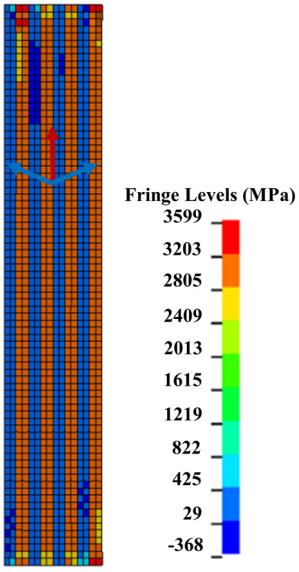

Figure 11.—Contours of stress in the axial tow (red arrow) direction.

The stress-strain curve for the 30° off-axis tension simulation as well as the experimental data can be seen in Figure 10(b). The strength predicted by the simulation, taken to be the stress at the first load drop, of approximately 580 MPa is slightly higher than the two experimentally measured strength values of 450 and 520 MPa. It should be noted that in Cater et al. (2015), the predicted strength of the 30° straight-sided coupon was approximately 500 MPa. The difference can be attributed to using one layer of shell elements through the thickness instead of six and different stress limiting parameters. As mentioned earlier, this slight loss in accuracy in simulating the quasi-static coupon response was deemed acceptable in order to be able to effectively apply this analysis approach to impact simulations. Despite the discrepancy in predicted strength from the experimental values, the predicted failure mode agrees with the experimental failure mode, which was identified by Cater et al. (2015) to be a longitudinal compressive failure of the bias tows oriented perpendicular to the applied loading. The damage in the simulation initiates at the edge of the gage section of the coupon then progresses in the direction of the axial tows, which is in agreement with the experiment. One notable difference between the simulation and the experiment is that the damage in the experiment was localized near the path of one axial tow in the gage section of the coupon whereas the damage in the simulation was visible in multiple locations throughout the gage section. Additionally, the simulated stress-strain curve indicates the 30° coupon is still able to carry additional load after the initial load drop. This is interesting since Cater et al. (2015) reported that, qualitatively, the 30° experimental coupon seemed to exhibit the highest post-failure residual stiffness compared to the other coupons. In the simulation, only the integration layers corresponding to +60° bias plies (oriented perpendicular to the applied loading) fail (in longitudinal compression). All other ply directions are undamaged, which is consistent with the fact that, in the experiment, the –60° bias tows and axial tows remained intact and continuous post-failure (Cater et al. 2015). Post-peak, the simulation indicates the –60° bias tows, the axial tows, and the remaining +60° bias tows (SLIMT1 = 0.3) carry the majority of the load.

Both the predicted strength and modulus of the 60° coupon are in good agreement with experimental data, as seen in Figure 10(c). In the simulation, damage initiates in the bias tows oriented perpendicular to the loading direction at the edge of the coupon near the grips and progresses to the other side of the coupon in the direction of the axial tows. The damage is localized near the grips and is not visible in the gage section. The simulation is in good agreement with the experimental failure mode, which was identified by Cater et al. (2015) to be a longitudinal failure of the bias tows oriented parallel to the applied loading, and failure path, which was in the direction of the axial tows. An image of a tested 60° off-axis tension coupon can be seen in Figure 12. It can be seen that the failure path is in the direction of the axial tows. Simulated contours of damage in the (local) longitudinal direction can be seen in Figure 13. The red (fully damaged) elements correspond to integration layers that represent the bias plies oriented parallel to the applied loading (the local longitudinal direction of the failed bias plies) and it can be seen that the row of red elements is along the direction of the axial tows. After the load drop in the simulation, the remaining coupon strength is due to the remaining strength left in the failed –60° bias tows, which can still carry 30 percent of their ultimate longitudinal tensile strength after failing in longitudinal tension (SLIMT1 = 0.3).

The stress-strain curve for the 90° transverse tension coupon simulation is shown in Figure 10(d). The simulated results are in good agreement with those obtained in Cater et al. (2015). However, the predicted strength, modulus, and failure mode do not agree with the experimental results. Due to this, the simulated post-peak response is likely numerical artifact. The simulation predicts a longitudinal tensile failure of the bias tows whereas an edge initiated shear failure was observed to propagate along the direction of the bias and axial tows in the experiments (Kohlman 2012). A limitation of the mesh discretization used in this study is the lack of continuity of the bias tows, effectively making it more difficult to model phenomena driven by the behavior of ungripped fibers. The next section discusses the failure modes of the notched coupon experiments, which were designed to mitigate the said free edge effects associated with straight-sided transverse tension coupons.

Figure 12.—Failed 60° off-axis tension coupon.

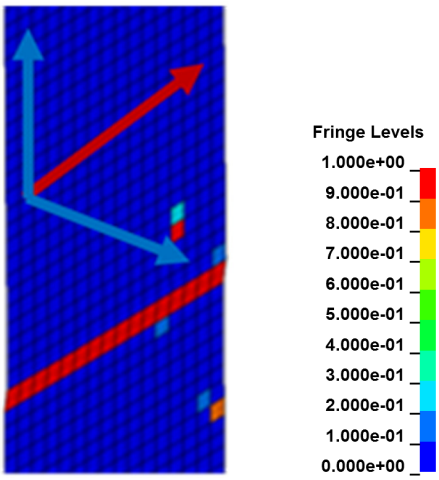

Figure 13.—Contours of damage in the local longitudinal direction.

Notched Coupon Experimental Failure Modes

In order to facilitate tensile failure in transverse tension tests and obtain improved transverse tensile strength values, notched coupon geometry was designed to allow all the bias tows in the gage section to be gripped during transverse tension tests (Kohlman 2012). This notched coupon geometry effectively mitigated the aforementioned edge initiated shear failure (due to the bias tow termination at the free edges) observed in straight-sided transverse tension tests. Given the variety of strengths and failure modes observed in the straight-sided experiments, a full suite of notched tensile coupon experiments were conducted for loading directions 0°, 30°, 60°, and 90° with respect to the axial tows. As with the straight-sided coupons, the axial (0°) and transverse (90°) notched tension tests load the coupons in directions parallel and perpendicular to the axial tows whereas the 60° and 30° off-axis notched tension tests load the coupons in directions parallel and perpendicular to the bias tows.

The same MTS servo hydraulic load frame used for the straight-sided coupon tests was used to load the notched coupons at a displacement rate of 1.27 mm/min. The physical notched coupons under investigation are 152.4 mm in length, 76.2 mm in width, and 3.175 mm in thickness. The notches are 1.3 mm wide and are located in the center of the coupons with 35.8 mm between the notch tips. During the tests, the load frame gripped 50.8 mm on each end of the coupons (with no tabbing used), leaving a 50.8 mm gage length. This section discusses the experimental failure modes observed in the notched coupon tension tests.

The failure mode in 0° notched axial tension experiments was identified to be a tensile failure of the axial tows oriented parallel to the applied loading; the same failure mode was identified in straight-sided axial tension experiments. A failed notched axial tension coupon is shown in Figure 14(a). Though both the straight-sided and notched axial tension experiments exhibited the same failure mode, the notched coupons exhibited a lower ultimate strength. Kohlman (2012) attributes this decrease in ultimate strength to early failure of the local axial tows near the notch tip(s) due to stress concentrations. The 30° notched off-axis tension coupons failed due to a tensile failure of the bias tows that are not oriented perpendicular to the applied loading. Notice that in Figure 14(b), the top half (above the notch) of the 30° coupon has shifted to the right. It is hypothesized that this is caused by the load transferring to the axial tows after the failure of the bias tows, causing them to align with the load direction and the top of the coupon to shift. Note that transverse tow splits can be seen in the bias tows oriented perpendicular to the applied loading.

The 60° notched off-axis tension coupons failed due to a tensile failure of the bias tows along the loading direction. As shown in Figure 14(c), damage initiates at the notch tip and propagates in the direction of the axial tows. It can be seen that the bias tows break at the points in which they undulate underneath the axial tows; there are stress concentrations at the point of undulation, but the tough PR520 resin will not allow debonding, so the bias tows fail. The 90° transverse tension coupon failed due to a tensile failure of the bias tows, just as they were designed to do (Kohlman 2012). It can be seen in Figure 14(d) that the majority of the damage is localized in between the notch tips.

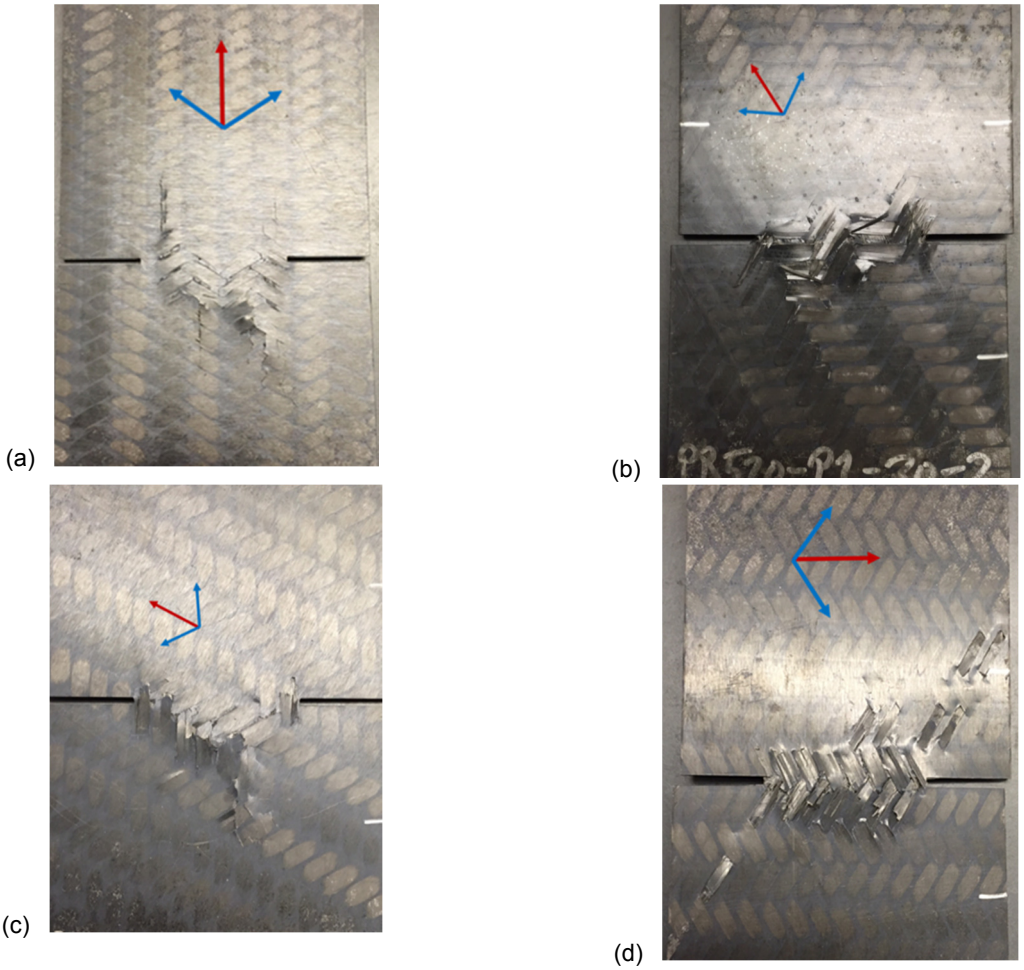

Figure 14.—Failed notched coupons; (a) 0°; (b) 30°; (c) 60°; (d) 90°.

Notched Coupon Simulation Results

The notched coupon tensile tests were simulated using the developed subcell model in order to evaluate the ability of the method to simulate the deformation response and damage patterns observed in the experiments. Note that the simulations have been conducted using the same material properties and parameters used in the straight-sided simulations. The finite element meshes of the 0°, 30°, 60°, and 90° off-axis notched tension coupons can be seen in Figure 15(a) to (d) and the simulated stress-strain curves are shown in Figure 16(a) to (d). Note that there are some elements near the notches with poor aspect ratios; these elements were assigned artificially high strengths so they did not cause early failure in the simulations. As previously mentioned, the simulated post-peak stress strain response shown in Figure 16(a) to (d) may primarily be numerical artifact.

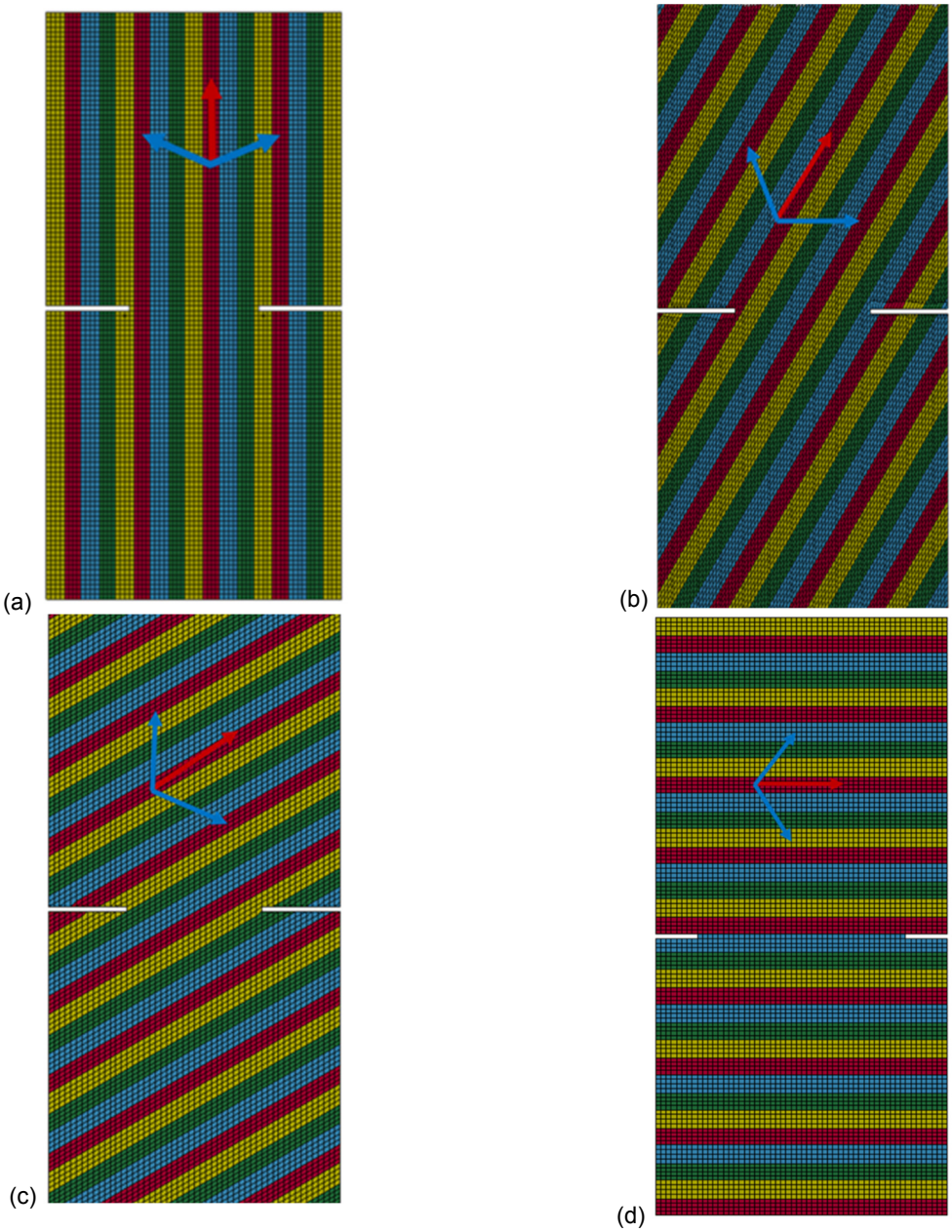

Figure 15.—Finite element models of the (a) 0°, (b) 30°, (c) 60°, and (d) 90° notched coupons created in LS-DYNA.

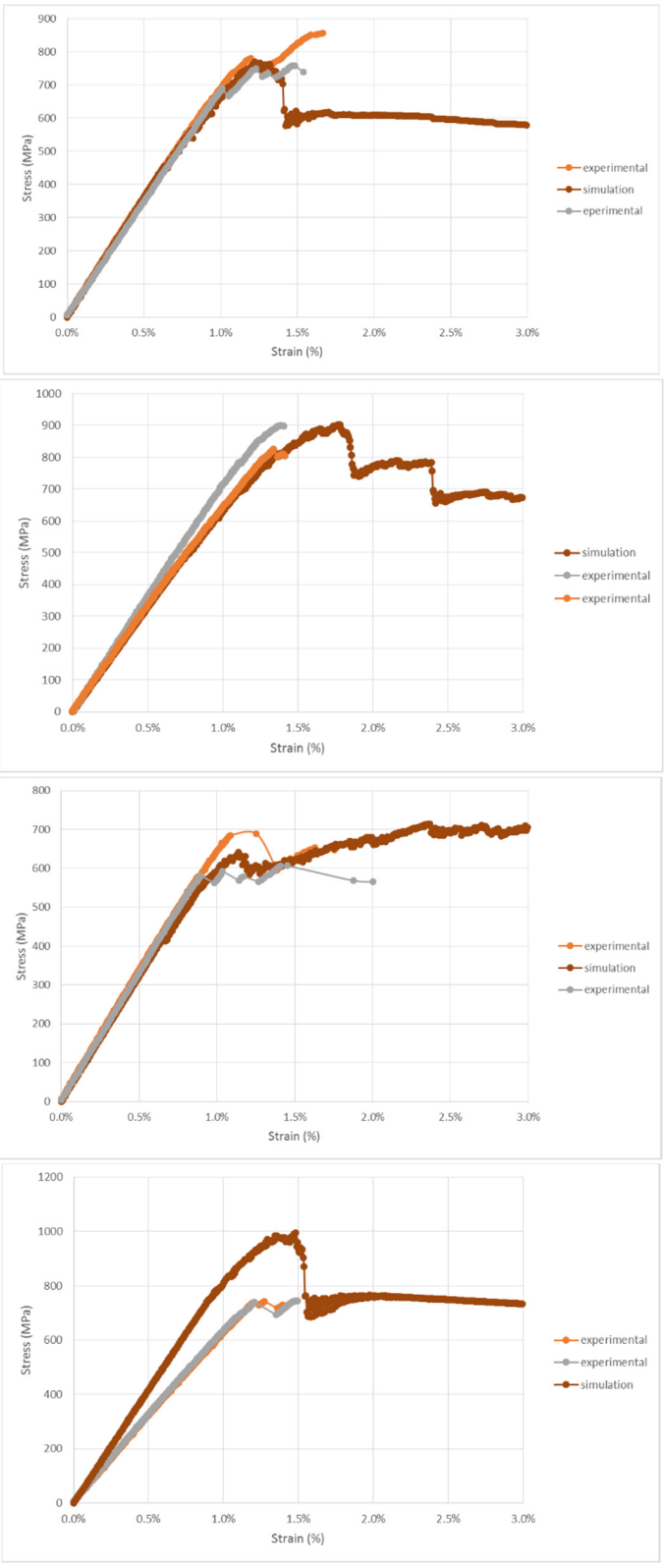

Figure 16.—Stress-strain curves for notched coupon simulations; (a) 0° axial tension; (b) 30° off-axis tension; (c) 60° off-axis tension; (d) 90° transverse tension.

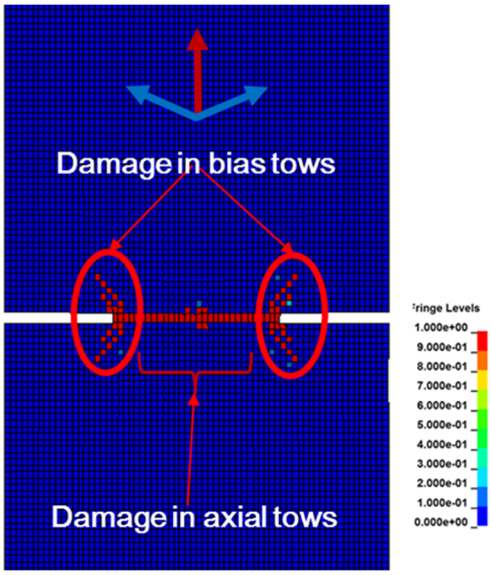

Figure 17.—Contour plot of the maximum value of (local) longitudinal damage in 0° notched coupon just after the global load drop.

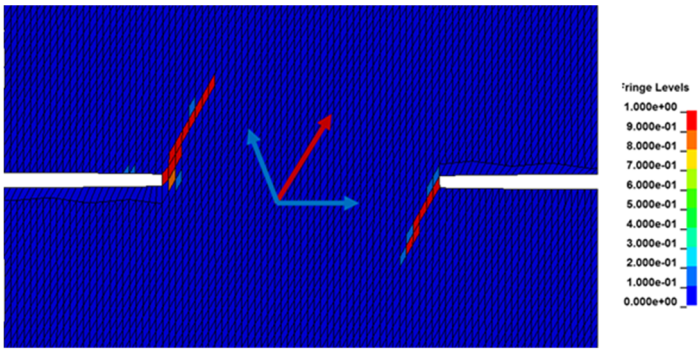

Figure 18.—Contour plot showing the maximum value of (local) longitudinal damage in the 30° notched coupon prior to failure; damage initiates at the notch tips and progresses in the direction of the axial tows.

The predicted strength and slope of the stress-strain curve up to 0.2 percent strain of the 0° notched axial tension coupon are 770 MPa and 73 GPa, respectively. The predicted strength is in good agreement with the experimental strengths of 688 and 780 MPa. Note in this study that the stress at the first slight drop in load was considered to be the strength, both for simulations and experiments. The stress-strain response also compares quite well to the experiment, as can be seen in Figure 16(a). In the simulation, damage initiates in the axial tows near the notch tips (parallel to the applied loading) at approximately 0.8 percent strain. The damage in the axial tows then progresses from notch tip to notch tip. The axial tows closest to the notch tip fail in tension first, which causes the majority of the load to be transferred to the remaining axial tows followed by subsequent tensile failure. After the drop in load in the simulation, the majority of the load is carried by what remains of the axial tows; this is likely numerical artifact. A contour plot of the maximum value of damage in the (local) longitudinal direction immediately following the global load drop can be seen in Figure 17. The red elements are elements with one or more fully damaged integration layer(s). The majority of the damage corresponds to the axial tows, though some damage in the bias tows is observed.

The predicted strength and slope of the stress-strain curve up to 0.2 percent strain of the 30° notched tension coupon are 903 MPa and 66 GPa, respectively. This compares well to the experimentally measured strength values of 825 and 900 MPa. It can be seen in Figure 16(b) that the stress-strain response of the simulation more closely matches with the orange experimental stress-strain curve, whereas the predicted strength more closely matches with the grey experimental stress-strain curve. Damage in the simulation initiates in the bias tows that are offset from (not oriented perpendicular to) the applied loading at the notch tips at approximately 0.5 percent strain. These tows are in tension. The damage then progresses in the direction of the axial tows, as shown in Figure 18. Note that the contour plot in Figure 18 shows the *maximum* value of damage in the (local) longitudinal direction, so the fully damaged (red) elements are not necessarily in the same integration layer (and thus do not necessarily correspond to the same ply regions). In fact, the damage corresponds to both –60° bias tows in tension as well as +60° bias tows in compression due to Poisson's effect. At a strain level of approximately 1.7 percent (just prior to failure), damage in the axial tows initiates at the left notch tip and progresses towards the right notch tip. As these axial tows fail, the nearby –60° bias tows (not oriented perpendicular

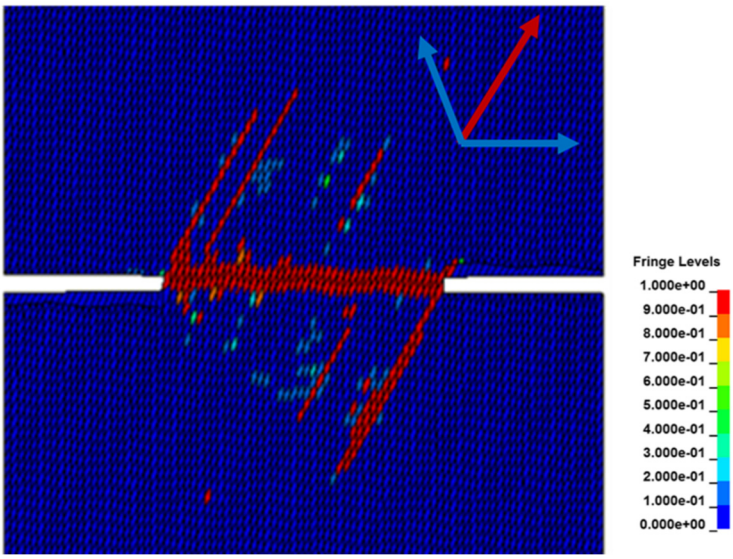

Figure 19.—Contour plot of the maximum value of (local) longitudinal damage in the 30° coupon just after failure.

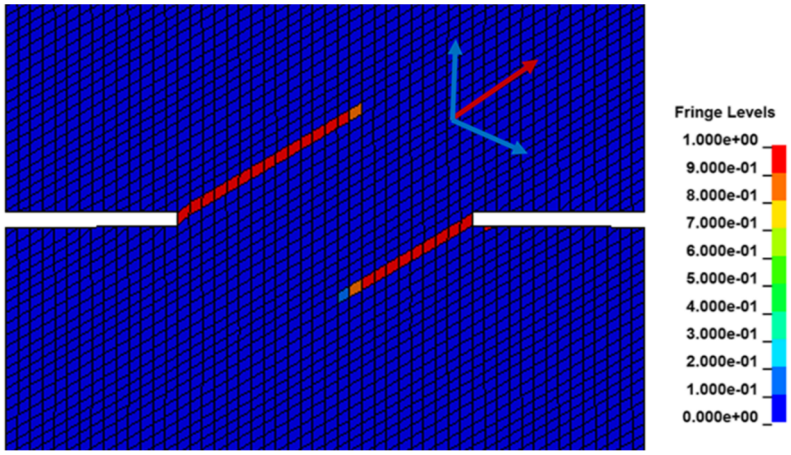

Figure 20.—Contour plot of maximum value of (local) longitudinal damage in the 60° notched coupon just after the load drop; all damaged (red) elements correspond to bias tows oriented parallel to the applied loading, which are in tension.

to the applied loading) also fail in longitudinal tension. The load drop in the simulation does not occur until all the axial tows between the notch tips have failed in tension. Thus, the predicted failure mode is a combined tensile failure of the bias tows offset from (*not* oriented perpendicular to) the applied loading and the axial tows. Note that this slightly differs from the experimentally observed failure mode, which was identified as a tensile failure of the bias tows. After the load drop in the simulation, the load is primarily carried by –60° bias and axial tows. Figure 19 shows a contour plot of the maximum value of damage in the longitudinal direction just after failure.

The predicted strength and slope of the stress-strain curve up to 0.2 percent strain for the 60° off-axis notched tension coupon are 642 MPa and 64 GPa, respectively. The predicted strength compares well to the experimentally measured strength values of 581 and 685 MPa. The predicted stress-strain response also compares well to the two experimental stress-strain curves, as shown in Figure 16(c). Damage initiates at the notch tips in the bias tows that are aligned with the applied loading and progresses in the direction of the axial tows. Figure 20 shows contours of the maximum value of (local) longitudinal damage just after the load drop. This damage is only visible on the integration layers that correspond to

–60° bias tows. Thus, the predicted failure mode is a tensile failure of the bias tows oriented parallel to the applied loading, which agrees with the experimental failure mode. It should be noted that after the initial load drop, the 60° coupon simulation continued to take additional load, as can be seen in Figure 16(c). The simulation indicates that the axial tows carry the majority of the load after the load drop. Since the first load drop is only due to the –60° bias tows failing in longitudinal tension, the (relatively) undamaged axial tows allow the coupon to take additional load.

The predicted strength and slope of the stress-strain curve up to 0.2 percent strain of the 90° notched transverse tension coupon are 994 MPa and 84 GPa, respectively. Unlike the 0°, 30°, and 60° notched coupon simulations, the predicted strength does not agree well with the experimentally measured strength of 740 MPa, as seen in Figure 16(d). However, previous works (Kohlman 2012) have indicated that, ideally, the transverse tensile strength should approximately equal the axial tensile strength. Thus, while the subcell model may not be able to match the experimental response, possibly due to local details that the model cannot currently simulate, it may be capturing what is the true large field strength of the material. In the simulation, damage initiates in the bias tows (both +60° and –60°) at the notch tips at about 1.1 percent strain and progresses in the global transverse direction (from notch tip to notch tip). Simulated contours of the maximum value of damage in the (local) longitudinal direction just after the load drop are shown in Figure 21. The damage is highly localized between the notch tips. All the fully damaged (red) elements in Figure 21 correspond to integration layers that represent bias tows. Thus, despite the fact the predicted strength and stress-strain response deviate significantly from the experiments, the predicted failure mode is a tensile failure of the bias tows, which agrees well with the experiment. Though it is likely numerical artifact, after the drop in load, most of the load is carried by the remaining bias tows in their longitudinal direction and the axial tows in their transverse direction.

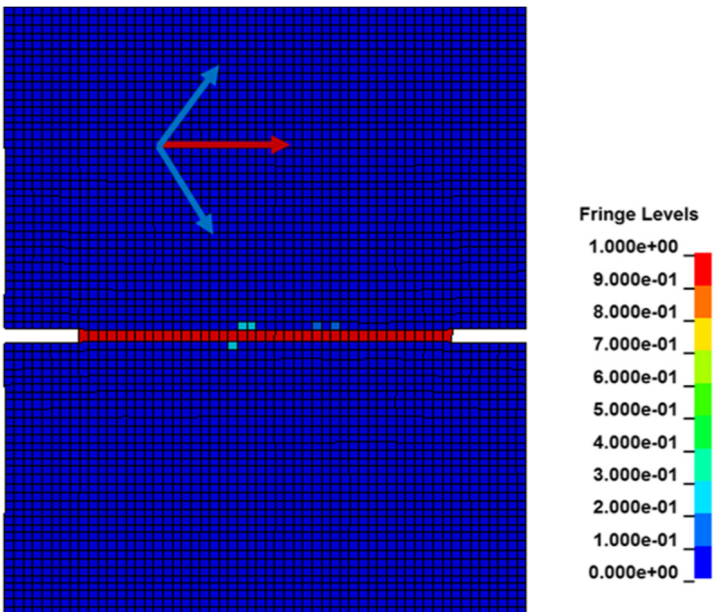

Figure 21.—Contour plot of maximum value of (local) longitudinal damage just after global load drop; fully damaged (red) elements correspond to bias tows that have failed in tension.

Conclusion

The subcell model, a semi-analytical modeling approach developed to allow for computationally efficient analysis of textile composites, including architectural effects, was tested by analyzing the deformation response and damage initiation and propagation in both straight-sided and notched quasi-static tension tests of a representative braided composite with a [0°/60°/–60°] braid architecture. The straight-sided and notched coupons were loaded at a variety of off-axis angles (0°, 30°, 60°, and 90°) with respect to the axial tows. The axial (0°) and transverse (90°) tension tests loaded the coupons in directions parallel and perpendicular to the axial tows whereas the 60° and 30° off-axis tension tests loaded the coupons in directions parallel and perpendicular to the bias tows. Model parameters (strengths and stiffness properties) were obtained using available top-down unit cell and bottom-up micromechanics techniques. The predicted strength and failure modes of the 0°, 30°, and 60° off-axis straight-sided coupon simulations were found to agree well with experiments. However, the predicted strength and failure mode of the straight-sided transverse tension simulations did not agree with the experiments because the edge initiated shear failure observed in experiments is not modeled in the numerical model. The notched coupon simulations also agree well with experiments in terms of strength and failure mode, though the strength was over predicted for the transverse (90°) tension simulation. Previous work modeled the coupons for the quasi-static tension simulations with six layers of composite shell elements through the thickness, each with three integration layers. However, preliminary flat panel impact simulations yielded nonphysical results when modeling with six layers of shell elements through the panel thickness. Thus, in this work the coupons were modeled with one layer of shell elements, with 18 integration layers, through the thickness. Slight discrepancies in experimental results compared to previous research were observed, the most notable being an increase in predicted modulus for the straight-sided axial (0°) tension simulation. These slight discrepancies, however, were deemed acceptable in order to allow the subcell model to work properly for impact simulations. Future work involves conducting flat panel impact simulations as well as generalizing the subcell methodology such that other general textile architectures other than a triaxial braid may be analyzed. Overall, the subcell method shows promise in providing a tool to allow for improved impact modeling of composites with complex fiber architectures.

References

Bednarcyk, B.A. and Arnold, S.M., "MAC/GMC 4.0 User's Manual—Keywords Manual," NASA TM-212077, 2002.

Bednarcyk, B.A., and Arnold, S.M. (2003). Micromechanics-based modeling of woven polymer matrix composites. *AIAA journal*, *41*(9), 1788–1796.

Blinzler, B.J., "Systematic approach to simulating impact for triaxially braided composites," Ph.D. Dissertation, Department of Civil Engineering, University of Akron, Akron, OH, 2012.

Cater, C.R., et al. "Single Ply and Multi-Ply Braided Composite Response Predictions Using Modified Subcell Approach," *Journal of Aerospace Engineering* (2014): 04014117. DOI: 10.1061/(ASCE)AS.1943-5525.0000445.

Cater, C.R., Xiao, X., Goldberg, R.K., and Kohlman, L.W. "Experimental and Numerical Analysis of Triaxially Braided Composites Utilizing a Modified Subcell Modeling Approach," NASA TM-18814, 2015.

Cheng, J. (2006). *Material modeling of strain rate dependent polymer and 2D tri-axially braided composites* (Doctoral dissertation, The University of Akron).

Cheng, J., and Binienda, W.K., "Simplified braiding through integration points model for triaxially braided composites," *Journal of Aerospace Engineering* 21.3 (2008): 152–161.

Chou, T.W., and Ishikawa, T. (1983). One-dimensional micromechanical analysis of woven fabric composites. *AIAA journal*, *21*(12), 1714–1721.

Goldberg, R.K., Blinzler, B.J., and Binienda, W.K., "Modification of a Macromechanical Finite Element–Based Model for Impact Analysis of Triaxially Braided Composites." *Journal of Aerospace Engineering* (2011).

Goldberg, R.K., Roberts, G.D., and Gilat A., "Implementation of an associative flow rule including hydrostatic stress effects into the high strain rate deformation analysis of polymer matrix composites." *Journal of Aerospace Engineering* 18.1 (2003): 18–27.

Hahn, H.T., and Pandey, R. (1994). A micromechanics model for thermoelastic properties of plain weave fabric composites. *Journal of engineering materials and technology*, *116*(4), 517–523.

Hallal, A., Younes, R., and Fardoun, F. (2013). Review and comparative study of analytical modeling for the elastic properties of textile composites. *Composites Part B: Engineering*, *50*, 22–31.

Hallquist, J.Q., "LS-DYNA® Keyword User's Manual," Volume II Material Models, Version 971, Livermore Software Technology Company, Livermore, CA, 2006.

Hashin, Z. "Failure criteria for unidirectional fiber composites," *Journal of applied mechanics* 47.2 (1980): 329–334.

Ishikawa, T., and Chou, T.W. (1982). Stiffness and strength behaviour of woven fabric composites. *Journal of Materials Science*, *17*(11), 3211–3220.

Kohlman, L.W., "Evaluation of test methods for triaxial braid composites and the development of a large multiaxial test frame for validation using braided tube specimens," Ph.D. Dissertation, Department of Civil Engineering, University of Akron, Akron, OH, 2012.

Li, X., Binienda W.K., and Littell, J.D., "Methodology for impact modeling of triaxial braided composites using shell elements." *Journal of Aerospace Engineering* 22.3 (2009): 310–317.

Liu, K.C., Chattopadhyay, A., Bednarcyk, B., and Arnold, S.M. (2011). Efficient multiscale modeling framework for triaxially braided composites using generalized method of cells. *Journal of Aerospace Engineering*, *24*(2), 162–169.

Matzenmiller, A.L. J.T.R., Lubliner, J., and Taylor, R.L., "A constitutive model for anisotropic damage in fiber-composites." *Mechanics of materials* 20.2 (1995): 125–152.

Paley, M., and Aboudi, J., "Micromechanical analysis of composites by the generalized cells model." *Mechanics of Materials* 14.2 (1992): 127–139.

Pijaudier-Cabot, G., and Bazant, Z.P. (1987). Nonlocal damage theory. *Journal of engineering mechanics*, *113*(10), 1512–1533.

Roberts, G.D., Revilock, D.M., Binienda, W.K., Nie, W.Z., Mackenzie, S.B., and Todd, K.B. (2002). Impact testing and analysis of composites for aircraft engine fan cases. *Journal of Aerospace Engineering*, *15*(3), 104–110.

Schwer, L.E. (2011). A Brief Look at Mat_Non_Local: A Possible Cure for Erosion Illness? In *11th International LS_DYNA Users Conference* (Vol. 3, pp. 19–36).

Shokrieh, M.M., and Mazloomi, M.S. (2010). An analytical method for calculating stiffness of two-dimensional tri-axial braided composites. *Composite Structures*, *92*(12), 2901–2905.

Tanov, R., and Tabiei, A. (2001). Computationally efficient micromechanical models for woven fabric composite elastic moduli. *Journal of Applied Mechanics*, *68*(4), 553–560.

Xiao, X., et al. "Strength prediction of a triaxially braided composite." *Composites Part A: Applied Science and Manufacturing* 42.8 (2011): 1000–1006.

Yang, J.M., Ma, C.L., and Chou, T.W. (1986). Fiber inclination model of three-dimensional textile structural composites. *Journal of Composite Materials*, *20*(5), 472–484.